Comparison of biotite elastic properties recovered by spherical nanoindentations and atomistic simulations - influence of nano-scale defects in phyllosilicates

Eril Suhada Lanin[1], Hiroki Sone[1], Zheng Yu[1], Qitong Liu[1], and Bu Wang[1]

[1]University of Wisconsin-Madison

November 23, 2022

Abstract

Phyllosilicate minerals, due to their sheets structure and morphology, are known to cause anisotropy in bulk rock properties and make the bulk rock more compliant. Accurately characterizing the micromechanical behavior of phyllosilicate minerals from laboratory observations, which eventually translates to the bulk rock behavior, is still challenging due to their fine-grained nature. Recent advances in atomistic simulations open the possibility of theoretically investigating such mineral mechanical behavior. We compare the elastic properties of biotites recovered by spherical nanoindentation with those predicted from density functional theory (DFT) simulations to investigate to what extent theoretical predictions reproduce actual phyllosilicate properties. Spherical nanoindentation was conducted using schist rocks from Poorman Formation, South Dakota, USA, to recover continuous indentation stress-strain curves. Loading in the layer-normal orientation shows an average indentation modulus (M) of about 35 GPa, while loading in the layer-parallel orientation gives a higher average of about 95 GPa. To facilitate comparison, the elastic stiffness constants (c_{ij}) determined from DFT were converted to indentation modulus (M) using solutions proposed in this study. The majority of the nanoindentation modulus results are below the values inferred from the simulation results representing ideal defect-free minerals. We suggest that crystal defects present at the nano-scale, potentially ripplocations, are the dominant cause of the lower indentation modulus recovered from nanoindentation compared to those inferred from DFT simulations. Results highlight the importance of acknowledging the defects that exist down to the nano-scale as it modifies the mechanical properties of phyllosilicates compared to its pure defect-free form.

Comparison of biotite elastic properties recovered by spherical nanoindentations and atomistic simulations - influence of nano-scale defects in phyllosilicates

Eril Lanin[1*], Hiroki Sone[1], Zheng Yu[2], Qitong Liu[3], Bu Wang[3]

[1]Geological Engineering Program, Department of Civil and Environmental Engineering, University of Wisconsin-Madison.

[2]Department of Material Science and Engineering, University of Wisconsin-Madison.

[3]Department of Civil and Environmental Engineering, University of Wisconsin-Madison.

Corresponding author: Eril Lanin (lanin@wisc.edu)

Key Points:

- Elastic modulus of cleavage-free biotites, and their anisotropy, were measured using spherical nanoindentation.
- Density functional theory (DFT) was used to calculate the elastic stiffness constants of biotite polytypes.
- Modulus from nanoindentation were persistently lower than DFT prediction suggesting the prevalence of nano-scale crystal defects.

Abstract

Phyllosilicate minerals, due to their sheets structure and morphology, are known to cause anisotropy in bulk rock properties and make the bulk rock more compliant. Accurately characterizing the micromechanical behavior of phyllosilicate minerals from laboratory observations, which eventually translates to the bulk rock behavior, is still challenging due to their fine-grained nature. Recent advances in atomistic simulations open the possibility of theoretically investigating such mineral mechanical behavior. We compare the elastic properties of biotites recovered by spherical nanoindentation with those predicted from density functional theory (DFT) simulations to investigate to what extent theoretical predictions reproduce actual phyllosilicate properties. Spherical nanoindentation was conducted using schist rocks from Poorman Formation, South Dakota, USA, to recover continuous indentation stress-strain curves. Loading in the layer-normal orientation shows an average indentation modulus (M) of about 35 GPa, while loading in the layer-parallel orientation gives a higher average of about 95 GPa. To facilitate comparison, the elastic stiffness constants (c_{ij}) determined from DFT were converted to indentation modulus (M) using solutions proposed in this study. The majority of the nanoindentation modulus results are below the values inferred from the simulation results representing ideal defect-free minerals. We suggest that crystal defects present at the nano-scale, potentially ripplocations, are the dominant cause of the lower indentation modulus recovered from nanoindentation compared to those inferred from DFT simulations. Results highlight the importance of acknowledging the defects that exist down to the nano-scale as it modifies the mechanical properties of phyllosilicates compared to its pure defect-free form.

1 Introduction

As one of the most common minerals composing felsic to intermediate rocks, phyllosilicate minerals oftentimes hold an important control on the mechanical behavior of rocks. Due to their sheet structure, morphology, and the porous aggregate they form in sedimentary rocks, phyllosilicate minerals, including clays, micas, chlorites, and serpentine groups, are known to cause anisotropy in the bulk rock properties and make rocks more compliant and weaker with increasing phyllosilicate content. Phyllosilicates are also abundant in fault rocks and are believed to impose critical limits on the strength of crustal faults zones. Recently, the ductility of clay minerals in rocks is also receiving increasing attention because of its influence on productivity from hydrocarbon source rocks (e.g., shale gas, tight oil) (Dembicki and Madren, 2014), its ability to seal fractures (e.g., waste disposal) (Bock et al., 2010; Ingram and Urai, 2015), and ability to locally modify stress (Gunzberger and Cornet, 2007; Sone and Zoback, 2014b). However, studies on mechanical properties of clay minerals, or phyllosilicates minerals in general, are mostly limited to the bulk behavior of the clay-rich rocks because of the challenges in making quantitative measurements on fine-grained rocks at the grain scale. For example, with the exception of few studies on single crystal mica samples (Kronenberg et al., 1990), the micromechanics of how clay minerals promote plastic creep deformation of rocks is still described only phenomenologically (Sone and Zoback, 2014a; Trzeciak et al., 2018; Haghighat et al., 2020), and it is not understood whether inter-granular sliding or intra-granular deformation accommodates creep of clay-rich rocks. The mechanical properties of the phyllosilicates itself, as well as the micromechanics of how the mechanical behavior of phyllosilicates translates to the bulk rock behavior, is still a topic in need of further studies. Thus, reliable and quantitative techniques to observe the mechanical behaviors of clay minerals at the microscale are needed.

Several methods have been used to study the mechanical properties of phyllosilicate minerals, such as the acoustic method, Brillouin scattering method, multiple regression, atomistic simulation, and nanoindentation. The earliest effort can be traced back to the work of Aleksandrov and Ryzhova (1961), who derived pseudo-hexagonal or transversely isotropic (TI) stiffness constant of muscovite, biotite, and phlogopite minerals from ultrasonic techniques. Vaughan and Guggenheim (1986) measured the 13 elastic stiffness constants of muscovite by using Brillouin scattering. Militzer et al. (2011) derived a full elastic tensor of illite-smectite, muscovite, and kaolinite minerals based on density functional theory (DFT). Vyzkva et al. (2014) estimated the elastic properties of phyllosilicate minerals using multiple regression of a dataset compiled for various phyllosilicate minerals. A common aspect of these methods is that they recover moduli of the minerals at small strain magnitudes generated by acoustic waves or small perturbations in the model, which is orders less than the strain magnitude involved in static deformation of rocks relevant to various engineering settings.

Recent advancements of nanoindentation techniques have allowed the investigation of elastic moduli of single phyllosilicate grains at strain magnitudes relevant to static deformation. Zhang et al. (2009) used nanoindentation to study muscovite and rectorite, followed by studies on various 2:1 phyllosilicates (Zhang et al., 2010) and biotites (Lanin et al., 2019). These studies utilize the Berkovich indenter in which elastic moduli are extracted from the unloading phase of the experiment. An occasional shortcoming of the Berkovich indenter is that they introduce plastic deformation during the loading phase, before the unloading phase, which results in crack development around the indentation when working with brittle materials. Such cracking appears as the sudden increase in indentation depth without load increase in the loading phase known as pop-ins (Zhang et al., 2009; Lanin et al., 2019). These cracks can alter the effective elastic properties of the mineral volume investigated by the indenter, thus resulting in lower elastic moduli than the pure undamaged mineral (see comments from Bobko et al. 2009).

Meanwhile, the use of a spherical indenter helps to overcome these problems of a Berkovich indenter. Spherical indenters create less stress concentrations, thus less tendency for crack damage, and also allow the application of Hertz's contact theory (Hertz, 1881). More studies are utilizing spherical indenters to recover stress-strain data of the crack-free sample during the loading phase where deformation is purely elastic, as demonstrated by recent studies (Basu et al., 2009; Pathak and Kalidindi, 2015).

Another class of approach is to theoretically investigate the behavior of materials through atomistic modeling (e.g., molecular dynamic, density functional theory). These simulations allow one to study the mechanical behavior of materials that are otherwise difficult to recover due to technical and sample limitations in the laboratory. Modeling techniques are allowing us to directly study the dislocation processes, in some cases recovering estimates of activation energies for deformation (Yamakov et al., 2002; Domain and Monnet, 2005). However, careful discussion on the similarities and differences between modeled and actual materials is essential to properly extrapolate findings from the atomistic scale to the problem of interest.

In this study, we specifically focus on studying the behavior of biotite, as one example of a phyllosilicate, from nanoindentation tests using spherical indenter and density functional theory (DFT) simulations. Our objectives are to compare the anisotropic elastic properties of biotite measured by nanoindentation and estimated by atomistic simulations and also to understand the agreement and disagreement between the two approaches. Biotite minerals found in a low-porosity schist rock are used in the indentation study to ensure control over the orientation of the minerals. We first describe the experimental materials, the nanoindentation tests conducted, and the data analysis. We then describe the method and results of the atomistic simulations. Finally, we discuss the indentation modulus parameter, comparison between experiment and simulation results, and the possible cause of those differences.

2 Experimental materials and methods

2.1 Materials

The samples used in this study were schist rocks from the Poorman Formation collected from the Sanford Underground Research Facility (SURF), South Dakota, USA, collected under the kISMET project (Oldenburg et al., 2016, 2017), same as those used by (Vigilante et al., 2017). The rocks used in this study are characterized as a biotite-quartz-carbonate phyllite to schist (Caddey et al., 1991) also including chlorite and minor amounts of muscovite and rutile. These schist rocks were chosen because of their low porosity (less than 1%) and the large biotite grains (~100 microns) in the rock that allows us to probe single crystal properties. The presence of the biotite minerals within a rigid matrix, as opposed to a compliant micro-porous matrix of a lower-grade diagenesis rock, makes these schist rocks suitable for recovering the true mechanical properties of the biotite grains. Visual observation under a scanning electron microscope (SEM) shows that the biotite grains appear to be free of visible impurities and free of cleavages parallel to the (001) plane (Figure 1). These schist rocks also exhibit a well-defined and consistent foliation fabric visible to the eye, to which the biotite grains are aligned, which made it easier to control the orientation of the exposed biotite faces to study its anisotropy.

Two sets of small rectangular samples were prepared, whose largest faces were oriented parallel to the foliation (layer-normal loading) and perpendicular to the foliation (layer-parallel loading), and fixed in resin. The samples were then ground using sandpaper with different grit sizes, sequentially from 180, 320, 600, to 1200 grits. The ground surfaces were then polished using abrasives of 6 μm, 1 μm (diamond suspension), 0.5 μm (colloid alumina), and 0.04 μm (colloidal silica suspension) grain sizes, followed by inspections under the microscope after each polishing step to ensure no scratches were remaining from the previous polishing step. The sample preparation is completed by identifying the area of interest under an optical microscope and marking the area by giving a scratch mark. Then the exact positions of the mineral crystals of interest are identified under the SEM, as well as their relative position to the scratches so that the nanoindenter could later correctly probe the mineral crystals of interest.

The minerals within the area of interest were identified using Backscattered-Electron (BSE) imaging, point-shoot Energy-Dispersive X-ray Spectroscopy (EDS), EDS scanned images, and BSE-EDS stacked images. Two representative BSE-EDS images of layer-normal and layer-parallel loading samples used in the nanoindentation test are shown in Figure 1. As shown in Figure 1, the BSE-EDS image allows us to discriminate the biotite, chlorite, and muscovite layers down to the micron-scale, which are otherwise difficult to distinguish.

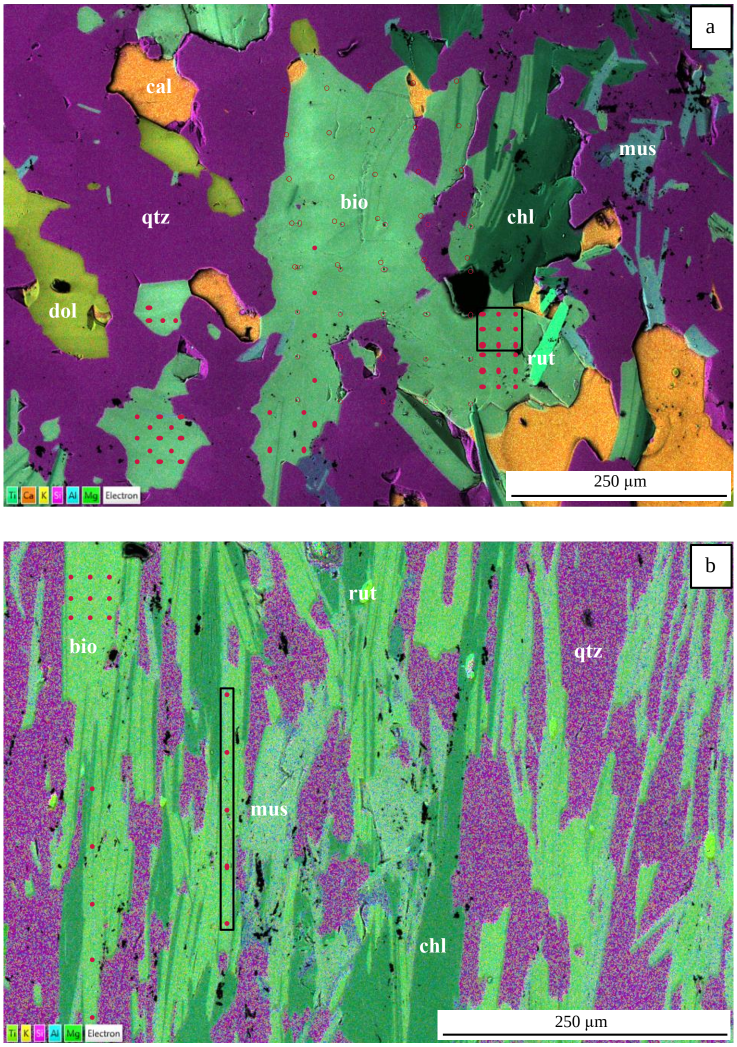

Figure 1 BSE-EDS stacked image of (a) layer-normal loading and (b) layer-parallel-loading. Abbreviations denote mineral names (bio=biotite, cal=calcite, chl=chlorite, dol=dolomite, mus=muscovite, qtz=quartz, rut=rutile). The circle markers represent the location where nanoindentation was perfomed. The squares show the dataset that recovered anomalously high and low modulus values in panel a and b, respectively.

2.2 Nanoindentation tests

Nanoindentation was carried out in areas of interest identified based on observations of the BSE-EDS image. Using the Hysitron TI-950 TriboIndenter capable of providing continuous stiffness measurement (CSM), the tests were performed at room temperature, in load-control mode, with maximum applied loads of 2-2.5 mN. Two diamond spherical indenters were used in these tests, whose tip radiuses were either 1 or 5 µm, with Young's modulus of 1.14 x 10^3 GPa and Poisson's ratio 0.007. The two tip radiuses were used to check whether one of the radii produces a better result in recovering elastic property compare to the other. In either case, results were screened, as explained later, so that only those recovering the proper elastic behavior is reported. Additionally, to understand the consistency and variability in the measurement results, indentation was performed in a grid pattern around the area of interest. To avoid interference between measurements, the grid interval was chosen to be greater than the indentation effect, which is approximately 2.4 times the indenter radius (Kalidindi and Pathak, 2008).

Until recently, majority of nanoindentation tests on rock-forming minerals were carried out using Berkovich indenters (e.g., Broz et al., 2006; Whitney et al., 2007; Zhang et al., 2009, 2010), with emphasis on extracting modulus and hardness values from the unloading mechanical data. However, since Berkovich indenters possess corners, nanoindentation tests using this type of indenters oftentimes result in brittle deformation almost instantaneously as soon as loading begins. Therefore, the information from the purely elastic mechanical response is not recovered, as well as the transition to the plastic regime. These problems can be mitigated using spherical indenters, where deformation at the purely elastic region and elastic-plastic transition can be observed by continuously measuring the contact stiffness and constructing the indentation stress-strain curves. Using Hertzian theory, contact stiffness measurements and the construction of indentation stress-strain curves can be carried out either with the use of multiple loading-unloading measurements (Field and Swain, 1996; Pathak et al., 2009) or with the use of the CSM technique (Herbert et al., 2001; Basu et al., 2006; Kalidindi and Pathak, 2008).

CSM is a technique carried out by superimposing, on top of the controlled load, a small oscillatory load with amplitudes about an order of magnitude lower than the applied load (Li and Bhushan, 2002). This technique is capable of continuously measuring the contact stiffness during a monotonic loading phase in a test without the need of carrying out multiple loading-unloading stages. On the Hysitron TI 950 Triboindenter machine, this CSM capability is referred to as the Continuous Measurement of X mode (CMX, where X is a mechanical property such as modulus, hardness, or stiffness), in the nano-Dynamic Mechanical Analysis (nano-DMA) module (Hysitron, 2014). Hereon, we will refer to the use of this CMX modes as the CSM modes as we are only interested in the mineral modulus in this study.

The experiments for this study were carried out with a linear load control (Linear CSM) consisting of 6 segments (Hysitron, 2014). As shown in Figure 2, segments 1-3 are the pre-loading phases, where the indenter contact with the specimen surface is established. The specimen is loaded in segment 4 using the Linear CSM mode. After the load is held for 2 seconds in segment 5, the specimen is unloaded in segment 6.

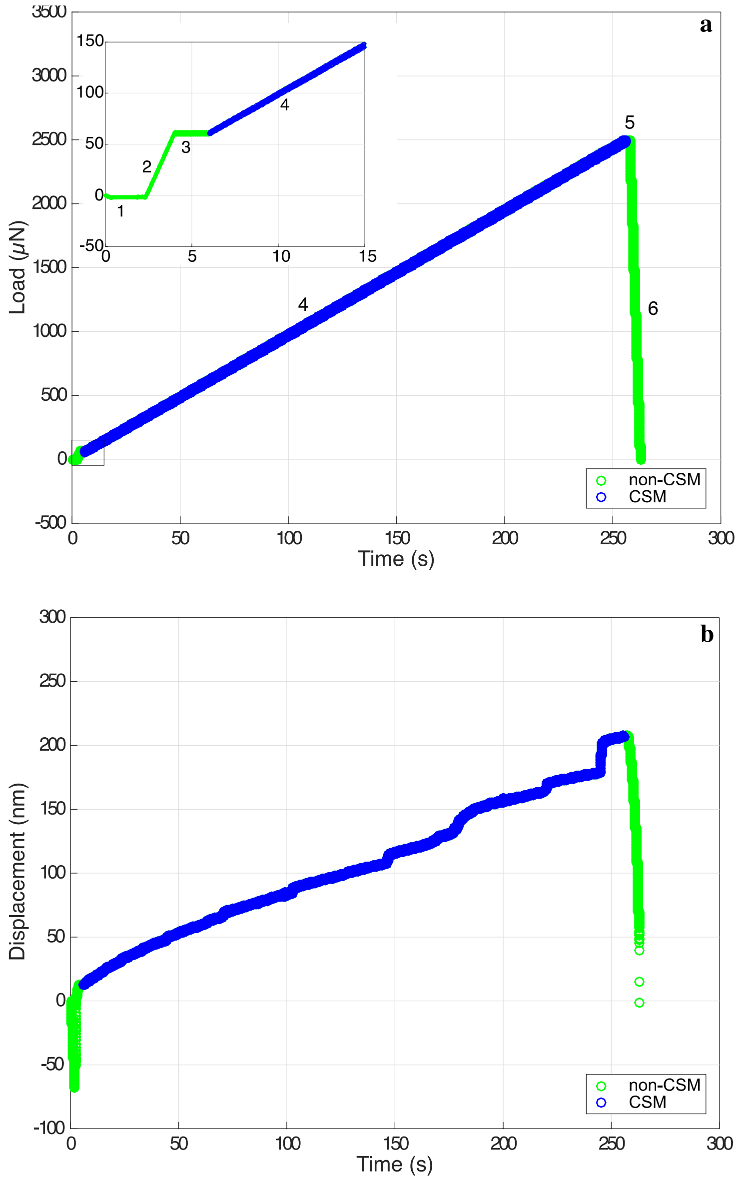

Figure 2 Example of nanoindentation data. (a) load vs. time and (b) displacement vs. time. Numbers represent the loading stages (1=hold phase, 2=intial loading phase, 3=hold phase, 4= CSM loading phase, 5=hold phase, 6=unloading phase).

2.3 Experimental data analysis

The current data analysis methods for nanoindentation data are based on Hertz's theory (Hertz, 1881; Johnson, 1985). According to Hertz's theory, the contact between two frictionless isotropic surfaces can be expressed as,

$$P = \frac{4}{3} E_r {R_r}^{1/2} {h_t}^{3/2}, \qquad a = \sqrt{R_r h_e} \tag{1}$$

where a is the radius of the contact boundary at any given load (P), h_t is the total indentation depth, and h_e is the elastic indentation depth (for a schematic explanation of the parameters used in this paper, please refer to Figure 3). E_r and R_r are the reduced modulus and the relative radius of indentation curvature, respectively, defined by,

$$\frac{1}{E_r} = \frac{1-\nu_s{}^2}{E_s} + \frac{1-\nu_i{}^2}{E_i}, \qquad \frac{1}{R_r} = \frac{1}{R_i} + \frac{1}{R_s} \tag{2}$$

where E and ν are the Young's modulus and Poisson's ratio, respectively, and the subscripts s and i refer to the sample and indenter, respectively.

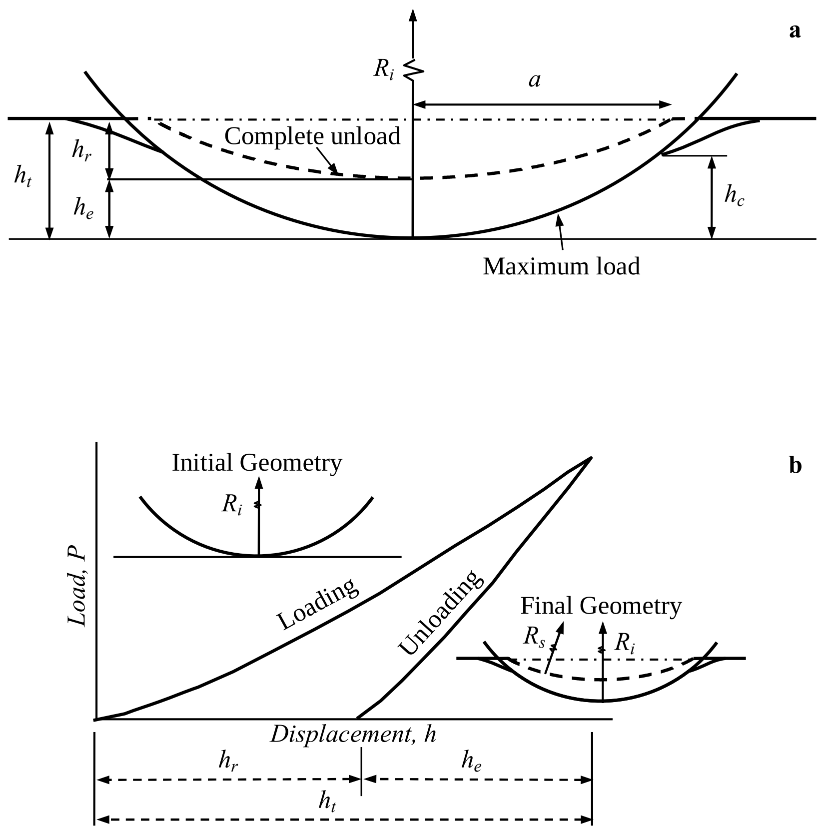

Figure 3 (a) Schematic of the indentation zone of spherical indenters. (b) Typical load-displacement curve with the initial and final contact geometry (modified from Kalidindi and Pathak, 2008). For the description of each parameter, refer to section 2.3. Experimental Data Analysis.

In the commonly employed approach described in Oliver and Pharr (1994, 2004), Hertz's model is applied to estimate Young's modulus of the tested material from the load-displacement curve. In their method, the elastic modulus is obtained from the unloading phase (segment 6), which is generally considered to be purely elastic. The reduced modulus is then calculated from Eq. (1) as

$$E_r = \frac{\sqrt{\pi}}{2}\frac{S}{\sqrt{A}} = \frac{S}{2a}, \qquad h_e = \frac{3}{2}\frac{P}{S} \tag{3}$$

where $S = dP/dh_e$ is the elastic stiffness, obtained as the slope of the unloading curve at initial or near the peak load, and $A = \pi a^2$ is the projected contact area. However, for reasons described in section 2.2, the elastic modulus of the material in this study was determined from data in the loading phase (segment 4). Referring to Pathak and Kalidindi (2015), the determination of elastic modulus with a spherical indenter involves a two-step process, including zero-point determination and construction of indentation stress-strain (ISS) curves.

2.3.1 Zero-point determination

Due to the very subtle change in load that occurs as the indenter initially contacts the sample (i.e. zero-point), together with other factors that falsely registers load before true contact (e.g. vibration, non-flat surface), it is difficult to determine the zero-point from load-displacement records. However, the correct identification of the zero-point is crucial for accurate determination of the specimen elastic modulus because it influences the estimation of the contact radius and the computed ISS significantly, which in turn will strongly affect the resulting elastic modulus. Several methods have been proposed by various authors to determine the zero point of the load-displacement curve from nanoindentation tests. Methods recently proposed for indentation apparatuses using CSM are from Moseson et al. (2008) and Kalidindi and Pathak (2008), whereas methods for apparatuses that do not use CSM are proposed by Pathak et al. (2009).

In the present study, using a nanoindentation machine with CSM capability, the zero-point determination was carried out by applying the Hertzian theory to Eq. (3) (Kalidindi and Pathak, 2008).

$$S = \frac{3P}{2h_e} = \frac{3(P' - P^*)}{2({h_e}' - {h_e}^*)} \tag{4}$$

where P', ${h_e}'$, and S are the measured load, displacement, and stiffness signal, respectively, from the CSM mode. P^* and ${h_e}^*$ are the load and displacement of the actual initial contact, respectively. By rearranging Eq. (4), one can establish a linear relationship between the quantities $P' - \frac{2}{3}S{h_e}'$ and S where the slope and y-intercept of the linear relationship represent quantities $-\frac{2}{3}{h_e}^*$ and P^*, respectively. Note that this relation only holds when the material response is still linearly elastic. Thus, by plotting the quantity $P' - \frac{2}{3}S{h_e}'$ against S recovered from the nanoindentation test, one can identify the initial portion of the data where the data resembles linear elastic behavior as well as recover the values P^* and ${h_e}^*$ necessary for zero-point determination (Figure 4).

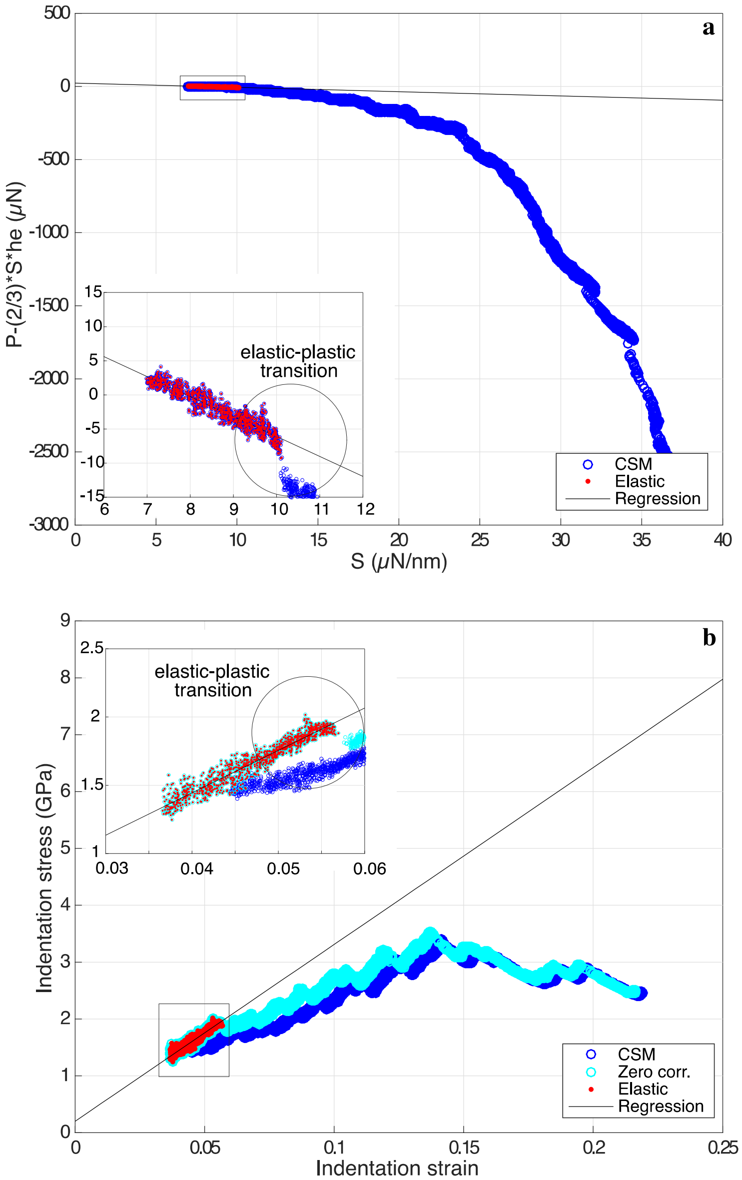

Figure 4 (a) Example of zero-point determination and (b) construction of indentation stress-strain. The blue circles show test data before zero correction and the cyan circle after correction. The red dots represent data of the elastic region, and the black line describes the linear regression.

2.3.2 Indentation stress-strain (ISS) curves

The use of indentation stress-strain curves has been introduced since the early development of the indentation technique by Tabor (1951). Indentation stress and strain is useful because it allows one to characterize the average stress-strain response of the material in the indentation zone although the stress and strain field is heterogeneous within the indentation zone. The methodology to extract indentation stress-strain curves from spherical indenter was first suggested by Field and Swain (1993). Currently, even though the definition of indentation stress is commonly accepted as,

$$\sigma_{ind} = \frac{P}{\pi a^2} \tag{5}$$

as used in various studies, there are two definitions of contact radius and strain proposed in the literature. The first definition is from Basu et al. (2006),

$$a = \sqrt{2R_i h_c - h_c^2}, \qquad \mathrm{e}_{ind} = \frac{4}{3\pi}\left(\frac{a}{R_i}\right) \tag{6}$$

which is similar to the one proposed by Herbert et al (2001), while the other definition proposed by Kalidindi and Pathak (2008) reads

$$a = \left(\frac{3PR_r}{4E_r}\right)^{1/3}, \qquad \mathrm{e}_{ind} = \frac{4}{3\pi}\left(\frac{h_t}{a}\right) \tag{7}$$

where σ_{ind} and e_{ind} are indentation stress and indentation strain, respectively, and $h_c = h_t - \frac{3}{4}\frac{P}{S} = h_t - \frac{1}{2}h_e$ is the effective contact depth.

The difference between the two definitions of strain and contact radius has been critically evaluated by Donohue et al. (2012). Even though the evaluation shows a distinct difference in the indentation stress-strain curves after the elastic-plastic transition, they show the same result when compared within the elastic regime regardless of the definitions being used. Therefore, for simplicity, the calculations of elastic property in this study use the definition by Basu et al. (2006) that uses known and directly measured parameters, namely the radius of the indenter, R_i, and penetration depth, h_t, as shown in Figure 3.

2.4 Experimental results

As an initial stage in the experimental data analysis, data screening was carried out to ensure that each data analyzed represent the elastic properties of biotite. Since the location of the indentation could not be controlled perfectly, the indentation locations were rechecked under the SEM to see whether the indentation were correctly placed on a biotite crystal or not. Indentation points located in other minerals or on the boundary between biotite and other minerals were excluded from the analysis. Additionally, further screening was conducted based on the plots of indentation stress and strain to check that the end of the elastic region is clearly marked by the elastic-plastic transition (Figure 4). Data with no clear elastic-plastic transition were not used in determining the elastic properties of biotite. After screening, linear regression to the indentation stress-strain data before the elastic-plastic transition allows us to recover the reduced modulus.

As a result of the screening process and validation, 48 indentation points in the layer-normal orientation and 17 indentation points in layer-parallel orientation were used to determine the elastic properties of biotite and the resulting values are shown in Table 1. In order to capture the variability of the resulting elastic modulus data from different data groups, we plot each indentation data in term of the (elastic) indentation stress and strain value at the elastic-plastic transition such that the slope of the line connecting to the origin would resemble the reduced modulus measured from each indentation (Figure 5).

Table 1 Summary of experimental reduced modulus (E_r) and indentation modulus (M)

Orientation	**Indenter Radius (um)**	**ID**	**Number of data**		**Er (GPa)**		**M (GPa)**	
			Indentation	**Screened**	**Mean**	**Sdev**	**Mean**	**Sdev**
Normal	1	N1-1	9	9	32.8	3.1	33.8	3.3
		N1-2	3	3	31.5	5.3	32.4	5.6
		N1-3	1	1	30.9		31.8	
		N1-4	9	9	32.3	2.3	33.3	2.5
		N1-5	4	4	29.7	2.1	30.5	2.3
		N1-6	4	4	33.0	4.8	34.0	5.1
		N1-7	9	7	51.4	6.1	53.9	6.7
	5	N5-1	9	3	33.6	12.8	34.7	13.6
		N5-2	5	4	31.5	5.4	32.4	5.7
		N5-3	4	4	30.8	7.1	31.7	7.4

Orientation	**Indenter Radius (um)**	**ID**	**Number of data**		**Er (GPa)**		**Ms (GPa)**	
			Indentation	**Screened**	**Mean**	**Sdev**	**Mean**	**Sdev**
Parallel	1	P1-1	9	9	92.6	24.8	101.4	29.6
	5	P5-1	5	4	62.4	15.1	66.2	17.1
		P5-2	5	4	105.8	5.2	116.6	6.3

For layer-normal loading, both 1 μm and 5 μm indenters showed a fairly consistent E_r value of about 32 +/- 5 GPa, except for the N1-7 dataset, which gave an average E_r of 51 +/- 6 GPa. Observation of the BSE-EDS image shows that there are no anomalous compositional variations seen under this N1-7 dataset, marked with a black box in Figure 1a. The N1-7 dataset was obtained close to the mineral boundary that transitions into a chlorite crystal and also surrounded by rutile and calcite minerals. Judging from how biotite and chlorite minerals are interlayered in Figure 1b, it is possible to speculate that the biotite was thinning towards this mineral boundary and potentially reflecting the stiffness of a stiffer underlying mineral continuing from the surrounding phases. Whether the anomalously high reduced modulus in N1-7 reflects the actual biotite property is unknown from available information.

Meanwhile, for the layer-parallel indentations, two datasets show a reduced modulus of about 96 +/- 21 GPa while another dataset (P5-1) gives an average of about 62 +/- 15 GPa. BSE-EDS image observations were also carried out to look for possible explanations of anomalies in this dataset, marked by the black box in Figure 1b. The BSE-EDS image shows that P5-1 is one of the two arrays of 5 indentation points which were placed within a thin biotite layer where fine inter-layering of biotite and chlorite occurs. A possible speculation is that weak mineral boundaries or cleavages unresolved in the BSE-EDS image may have influenced the results towards a low elastic modulus, but the reason is unknown from available information.

We observe consistently that the elastic limit for the 5 μm indenter data comes at a lower indentation stress and strain values compared to the 1 μm indenter data. We interpret this to be the result of the larger mineral volume that is probed by the larger indenter. For a given indentation strain value, the volume of investigation below the indenter will scale with the cube of the indenter tip diameter. Thus, there are greater chances for the 5 μm indenter to encounter pre-existing flaws in the mineral structure, if any, which leads to an earlier onset of plastic deformation and pop-ins. However, as long as we properly identify the elastic limit in the mechanical data, the reduced moduli values we recover at the elastic limit should not depend on the indenter tip radius assuming homogeneous mineral properties. Consistency between results from different indenter tip radius confirms that we were able to correctly identify the elastic plastic transition in the data.

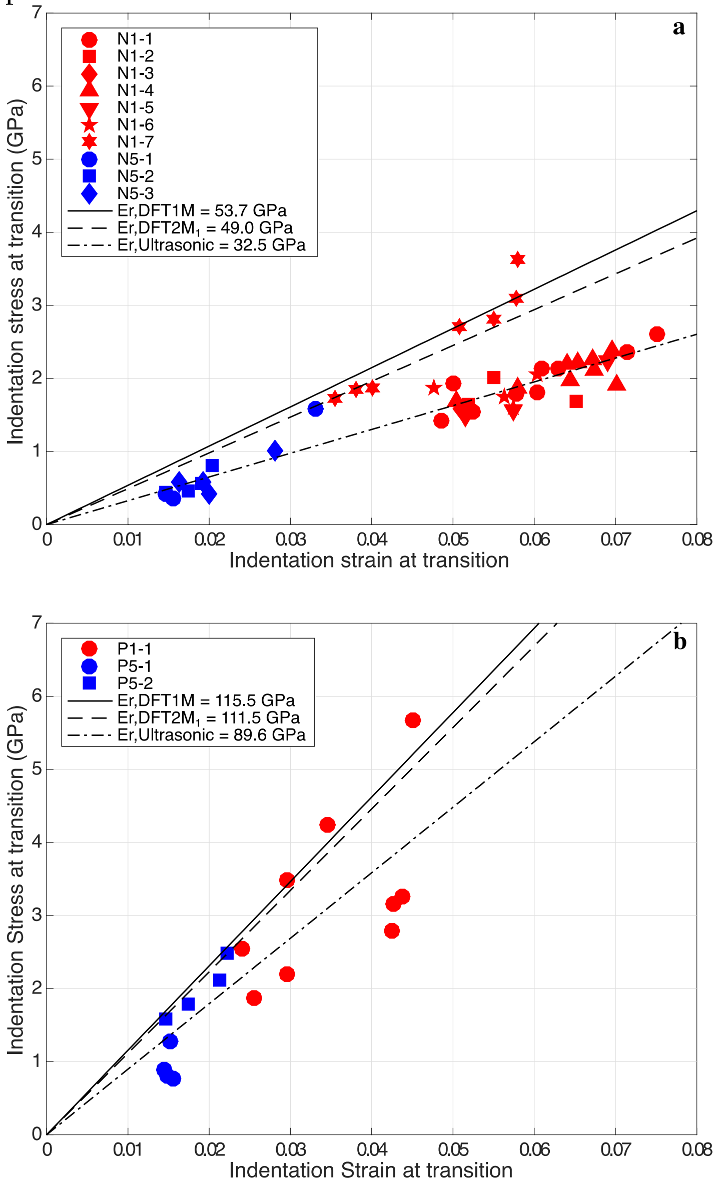

Figure 5 Indentation stress and indentation strain values at elastic-plastic transition for (a) layer-normal loading and (b) layer-parallel loading. Data from the tests using indenter with a radius of 5 μm is represented by a blue marker and 1 μm by a red marker. The different marker shapes depict different dataset groups. The lines describe stress-strain relations predicted by DFT and ultrasonic velocity measurements of Alksandrov and Ryzhova (1961).

Apart from biotite, to check the validity of the method used, analyses were also carried out on indentations that fell in quartz minerals. These serve as a quality control for our analysis considering that quartz minerals have nearly isotropic mechanical properties and their physical characteristics are widely known from previous studies. The 36 indentations located in quartz minerals give an average E_r value of 83.3 +/- 18.3 GPa. Based on Eq. (2), assuming that the Poisson's ratio of quartz is 0.07 (Mavko et al., 2009), this results in an average Young's modulus of 89.6 +/- 19.7 GPa. Considering that the Young's modulus of quartz is known to be about 94.5 GPa (Mavko et al., 2009), our method correctly recovers the known properties of quartz albeit with a large standard deviation.

3 Atomistic simulation methods and results

To offer a comparison with the nanoindentation measurements, the elastic properties of two common biotite polytypes, 1M and $2M_1$, were calculated from density functional theory (DFT) simulations. The atomic models of the two polytypes were constructed based on their crystal structures determined from X-ray diffraction experiments (Brigatti et al., 2000). As shown in Figure 6, the two polytypes have similar clay sheets separated by interlayer K^+, but with different stacking arrangements. In both polytypes, the clay sheets consist of an octahedral layer sandwiched between two tetrahedral layers. Diffraction experiments (Brigatti et al., 2000) have observed partial cation occupancies in both the octahedral and tetrahedral layers. Based on the experimental site occupancies, an ideal chemical composition of $K(Mg_2Al)(Si_3Al)O_{10}(OH)_2$ was adopted in this study. It should be noted, however, that substitution of Mg by Fe, Ti, Mn, etc. can exist in real samples to various degrees.

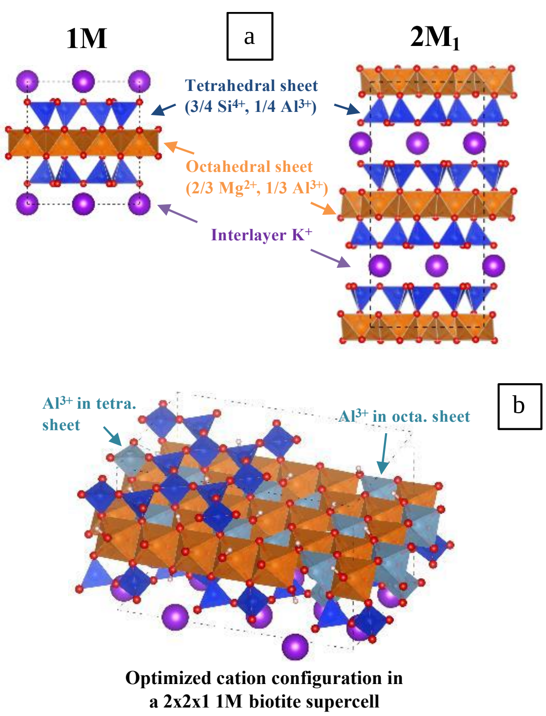

Figure 6 (a) Biotite polytypes and (b) optimized cation configuration in a 2x2x1 1M biotite supercell.

3.1 Simulation method

Although diffraction experiments suggested cation distributions in the clay sheets are disordered, explicit cation configurations were needed for computing elastic properties from DFT simulations. To this end, the cation arrangements in the clay sheets were first optimized in classical simulations. This was conducted using General Utility Lattice Program (GULP) (Gale, 1997) and ClayFF (Cygan et al., 2004), a classical force field that has been widely used for clay mineral simulations. Structural optimizations were performed for randomly generated cation arrangements in supercells of 1M and $2M_1$ polytype structures until no configuration with a lower energy can be found. Models with the most energetically favorable cation configurations, found in 2×2×1 and 2×1×1 supercells respectively for 1M and $2M_1$, were used for elastic property calculations. It should be noted that, although classical simulations using ClayFF offer accurate predictions for clay structures and energetics, they have been shown to overestimate the moduli of mica family clays by ~25% (Teich-McGoldrick et al., 2012). As such, the elastic properties were calculated from DFT simulations, using the atomic models of biotite with optimized cation arrangement.

The DFT simulations were conducted using the Vienna *ab initio* simulation (VASP) package with the projector-augmented wave pseudopotential of Blöchl (Blöchl, 1994; Kresse and Furthmüller, 1996). The generalized gradient approximation of Perdew-Burke-Ernzerhof was employed for the exchange-correlation functional (Perdew et al., 1996). Corrections for the van der Waals interactions were made with the DFT-D3 method with Becke-Johnson damping (Grimme et al., 2010, 2011). In all the calculations, the electronic wave function was expanded using a plane wave basis up to an energy cutoff of 520 eV. K-space meshes were set to ensure $a \times n_k > 20$ Å, where a is the lattice parameter and n_k is the number of k points along $2\pi/a$ in the reciprocal space. This results in a mesh of 2×1×2 for the 221 supercell of 1M. All lattice parameters and ionic positions were fully relaxed before mechanical property calculations. The convergence criterions for the energy during self-consistent field calculations and the force during structural relaxation were set as 10^{-6} eV and 0.005 eV/A, respectively. The elastic constants were calculated from the strain-stress relationship determined by relaxing the atomic positions under finite lattice distortions.

3.2 Simulation results

The elastic properties calculated from DFT simulations are listed in Table 2 together with those determined from ultrasonic measurements by Aleksandrov and Ryzhova (1961). Due to the explicit cation arrangements used in the atomic model, the structures deviate slightly from transverse isotropy. As such, small differences exist for both polytypes between simulated C11 and C22 and related properties. Nonetheless, the elastic properties from DFT simulations are in good agreement with ultrasonic measurements overall.

Table 2 Summary of elastic properties from simulation results and ultrasonic measurements.

Parameters	**Density Functional Theory (DFT)**		**Ultrasonic measurements***
	Biotite 1M	**Biotite $2M_1$**	**Unknown Polytype**
C11/C22	189/203	184/186	186
C33	60	56	54
C12	56	30	32.4
C13/C23	24/22	16/19	11.6
C44/C55	18/17	10/8	5.8
C66	71	100	76.8
E11/E22	167/182	204/233	178.6
E33	55	59	52.8
ν12/ν21	0.25/0.27	0.08/0.09	0.16
ν13/ν23	0.32/0.25	0.18/0.21	0.18
ν31/ν32	0.10/0.08	0.05/0.05	0.05

*Aleksandrov and Ryzhova (1961).

4 Discussion

4.1 Indentation modulus (M) for frictionless spherical indenters

Using the two-steps process as described in the data analysis section, the elastic modulus can be obtained in the form of a reduced modulus (E_r). However, because the Poisson's ratio of the samples (ν_s) is not measured by indentation, the reduced modulus (E_r) cannot be converted to Young's modulus of the sample (E_s) using Eq. (2), but only reported as indentation modulus (M). For an isotropic material, the general relation between Young's modulus (E) and Poisson's ratio (ν) with indentation modulus (M) is described as

$$M = \frac{E}{1 - \nu^2} \tag{8}$$

For anisotropic materials, however, the relationship between indentation modulus and Young's moduli is more complicated. Several methods have been proposed to determine the indentation modulus (M) for anisotropic materials. The effort started by the work of Willis (1966) who evaluated the problem for parabolic indenters using the contour integral. The simplified solution using the surface Green's function (Barnett and Lothe, 1975) was proposed by Vlassak and Nix (1993) for a flat circular punch, by Vlassak and Nix (1994) for Berkovich indenters, by Swadener and Phar (2001) and later refined by Vlassak et al. (2003) for conical and spherical indenters. The central concept in these methods involves deriving the indentation load-displacement function by integrating the material's Green's function over the contact area. However, it is generally difficult to obtain the exact forms of Green's function and contact area. Vlassak et al. (2003) provided a solution for indenters of arbitrary shape assuming the contact area is elliptical. For spherical indenter, the contact area is exactly elliptical, and the solution can be obtained using a Fourier expansion of the material's Green's function. Delafargue and Ulm (2004) further proposed a first-order approximation of the Green's function for indentations along or perpendicular to the axis of symmetry on a transversely isotropic solid. They derived solutions for conical indenters and demonstrated that the approximation yielded accurate results. The method was then, due to similarity of the sharp tip, used by the subsequent researcher (e.g., Ahmadov, 2011) to estimate the indentation modulus (M) for Berkovich indenter.

In our present study, the indentation modulus (M) is calculated based on the works of Vlassak, et al. (2003) and Delafargue and Ulm (2004). For a frictionless spherical indenter, the indentation modulus can be calculated based on Vlassak, et al. (2003) by:

$$M = \frac{1}{\alpha(e)(1-e^2)^{\frac{1}{4}}} \tag{9}$$

where:

$$\alpha(e) = \int_0^{\pi} \frac{H(\theta+\frac{\pi}{2})}{\sqrt{1-e^2\cos^2\theta}} \tag{10}$$

It is worth noting that both $\alpha(e)$ and the eccentricity e are related to the Green's function of the material, which can be written as:

$$H(\theta) = H_0 + H_{c1}\cos(2\theta) \tag{11}$$

where the two terms including H_0 and H_{c1} respectively represent the isotropic and anisotropic portions of the Green's function.

Since the indentations on the biotite samples were conducted either along or perpendicular to the axis of symmetry, we applied the first order approximation to the Green's function derived by Delafargue and Ulm (2004):

$$H_0 = \frac{H_2+H_3}{2}, \qquad H_{c1} = \frac{H_2-H_3}{2} \tag{12}$$

where H_2 and H_3 can be directly calculated from the elastic constants (c_{ij}):

$$H_2 = \frac{1}{2\pi}\sqrt{\frac{C_{3333}}{C_{11}C_{33}-C_{1133}^2}\left(\frac{1}{C_{1313}}+\frac{2}{\sqrt{C_{11}C_{33}}+C_{1133}}\right)}, \qquad H_3 = \frac{C_{1111}}{\pi(C_{1111}^2-C_{1122}^2)} \tag{13}$$

From here, the eccentricity of the contact area e and $\alpha(e)$ can be computed utilizing their relationship with the anisotropic ratio H_{c1}/H_0:

$$\frac{H_{c1}}{H_0} = \frac{(\partial/\partial e)(\alpha_0(e)\sqrt{2-e^2})}{(\partial/\partial e)(\alpha_2(e)\sqrt{2-e^2})} \tag{14}$$

where:

$$\alpha_0 = \int_0^{\pi} \frac{d\theta}{\sqrt{1-e^2\cos^2\theta}}, \quad \alpha_2 = \int_0^{\pi} \frac{\cos(2\theta)d\theta}{\sqrt{1-e^2\cos^2\theta}} \tag{15}$$

The eccentricity as a function of anisotropic ratio for spherical indenter is plotted in Figure 7. Once the eccentricity is determined based on biotite's elastic constants, the indentation modulus can then be calculated using Eq. (9-11).

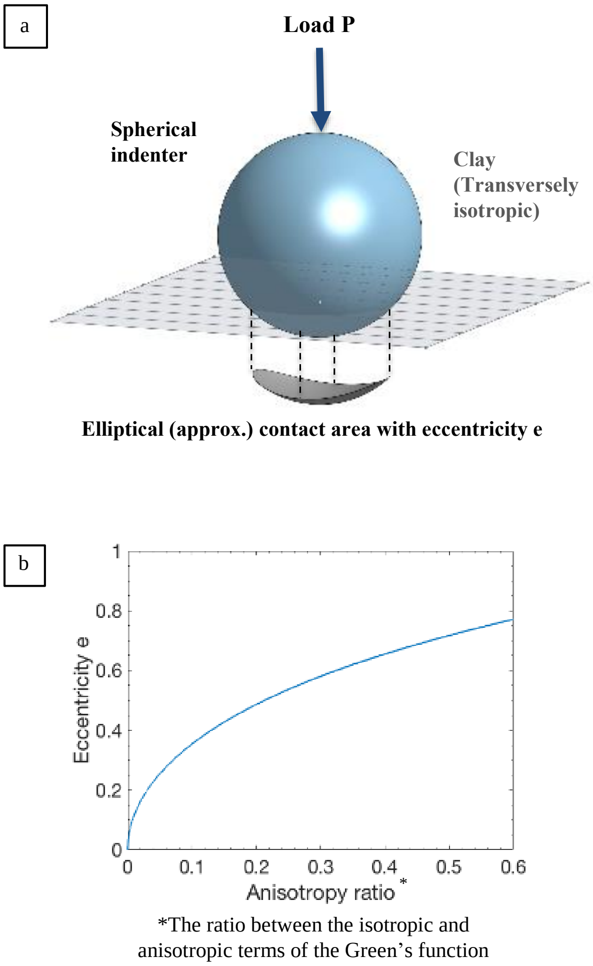

Figure 7 (a) Illustration of sperical indenter and (b) the relationship between eccentricity (e) with anisotropy ratio.

Based on these formulations, the elastic constant (c_{ij}) from DFT and ultrasonic method (Table 2) can be converted to indentation modulus (M) as presented in Table 3. Finally, the reduced modulus (E_r) is also calculated based on Eq. (2) from the indentation modulus (M) using the elastic properties of the diamond indenter tips.

Table 3 Indentation modulus (M) of DFT and ultrasonic measurements.

Method	**Polytype**	**Indentation Modulus (GPa)**		**Reduced Modulus[a] (GPa)**	
		Layer-normal	**Layer-parallel**	**Layer-normal**	**Layer-parallel**
Density Functional Theory (DFT)	1M	56.3	128.4	53.7	115.5
	2M1	51.2	123.4	49.0	111.5
Ultrasonic measurements[b]	Unknown	33.5	97.2	32.5	89.6

[a]Reduced modulus calculated from indentation modulus using diamond indenter properties of Young's modulus 1.14 x 10^3 GPa and Poisson's ratio 0.007. [b]Aleksandrov and Ryzhova (1961).

4.2 Comparison of experiments with simulation results

The elastic behaviors predicted by DFT and ultrasonic measurements are compared with experimental result in Figure 5 by drawing linear stress-strain relations whose slopes are determined by the reduced moduli calculated in the previous section (Table 3). We observe that nearly all experimental data plot on or below the DFT-simulated trends for both 1 μm and 5 μm diameter indenters. Thus the DFT prediction marks an upper bound to the elastic reduced moduli recovered from nanoindentation. The DFT predictions are slightly different between the two polytypes, 1M and $2M_1$, but the difference is small compared to the overall variation in experimental results. This suggests that the variability in experimental results are not explained by differences in polytypes.

Stress-strain relation predicted from the ultrasonic measurements by Aleksandrov and Ryzhova (1961) plot lower than those from the simulation reduced moduli, an obvious consequence of the lower indentation moduli recovered from the ultrasonic data. For the layer-normal loading dataset (Figure 5a), there appears to be a population of lower-moduli data that clusters along the ultrasonic-based trend, but not below. This may suggest that the ultrasonic-based modulus is the most compliant member when compared with DFT and nanoindentation results. For the layer-parallel loading dataset, there are less data points to confirm, but there is a population of nanoindentation results that plot below the ultrasonic-based trend therefore ultrasonic-based modulus does not appear to be the most compliant compared to DFT and nanoindentation results.

4.3 Causes of differences in simulation and experimental results

As reported above, in general, the reduced modulus (E_r) derived from nanoindentations distribute between those predicted from DFT simulations and the ultrasonic measurements by Aleksandrov and Ryzhova (1961), in both normal and parallel orientation. We suggest that these differences could be related to several causes, namely chemical impurities, cleavages, crystal defects, and scale dependence.

Chemical Impurities

The DFN simulations were carried out using the ideal chemical composition of a biotite ($K(Mg_2Al)(Si_3Al)O_{10}(OH)_2$), whereas biotite is known to be a continuous solid solution of Mg (magnesium) and Fe (iron), of which phlogopite is the Mg end-member and annite is the Fe end-member. The presence of Fe in the chemical composition of natural biotites may be responsible for the differences between the simulated and measured results. However, since Fe and Mg have the same number of cations ($^{+2}$) and bonding type, including Fe in the chemical composition of biotite is not expected to significantly change its mechanical properties. For comparison, Young modulus of biotite and phlogophite inferred from the ultrasonic velocities (Aleksandrov and Ryzhova, 1961) were 178.6 GPa and 169.8 GPa, respectively, in the layer-parallel direction, and 52.8 GPa and 48.8 GPa, respectively, in the layer-normal direction. We also did not observe a significant Fe peak compared to the Mg peak in the point-shoot EDS pattern recovered from biotite grains (1 cps/eV for Fe and 20 cps/eV for Mg). Therefore, chemical impurities are not expected to be the main cause of the discrepancy between the predicted and observed indentation moduli.

Closing of Cleavages

Because cleavages along the (001) basal plane are known to be prevalent in mica minerals, even in single crystal specimens, it is possible that the compliance observed in the ultrasonic and nanoindentation results are caused by the closing of the cleavage planes. However, this is unlikely the case at least for the nanoindentation data because: (1) no open cleavage planes were seen under the SEM in the biotite grains tightly embedded in the schist matrix, (2) closure of cleavages result in mineral stiffening but the linearity between the indentation stress and strain suggests no such stiffening, (3) closing of cleavage planes would not explain the low moduli also observed during layer-parallel loading. For the ultrasonic velocity measurement by Aleksandrov and Ryzhova (1961), Aleksandrov and Prodaivoda (1993) describes that the measurement was affected by cleavage planes. This may explain why ultrasonic-based reduced modulus for the layer-normal direction places at the lower-end of the range of reduced modulus exhibited by the nanoindentation results. We note that cleavages do not affect layer-parallel loading tests, so the low reduced modulus calculated from ultrasonic measurement compared to the DFT predictions requires a separate explanation.

Crystal Defects - Ripplocation

For the reduced modulus recovered from nanoindentation experiments, a more probable cause for the lower modulus compared to DFT results is the presence of defects in the crystal structures of biotite. The crystal structure used in the DFT simulations are of the ideal form of the polytypes 1M and $2M_1$, whereas the biotite samples used in the laboratory measurements, both ultrasonic velocity and nanoindentation, come from naturally occurring rocks. Naturally occurring minerals contain various defects known as vacancies and dislocations, which are critical ingredients for crystal plastic deformation of minerals at high temperatures (Poirier, 1985; Karato, 2008). Traditionally, the dominant mode of crystal defects in biotites have been thought to be dislocations parallel to the (001) basal plane, either along the biotite interlayer (Bell and Wilson, 1986; Kronenberg et al., 1990) or the within the oxygen layer between the octahedral and tetrahedral sheets (Noe and Veblen, 1999). But such dislocation do not accommodate out of plane movement of atoms, not plausible as an explanation for layer-normal compliance.

Recently, a new type of crystal defect in layered minerals, *ripplocation*, has been introduced by Kushima et al. (2015), which takes the form of atomic-scale ripple-like defects in the basal layer. Aslin et al. (2019) reports the abundance of nano-scale ripplocations in biotites found in a mylonite rock, as well as in an undeformed granite, observed under the TEM. Although we have not confirmed the presence of such defect features in the biotites we studied, we suggest that the low nanoindentation modulus is an evidence of the presence of ripplocations. The exact effect of such mineral defects on the elastic moduli of minerals is not known. But it is plausible that ripplocations reduce the stiffness of biotites in both layer-normal and layer-parallel direction because ripplocations can accommodate layer-normal expansion and layer-parallel shortening, similar to kink bands found in biotites (Aslin et al., 2019). Ripplocations would also explain the low reduced modulus in the layer-parallel direction estimated from ultrasonic measurements in the absence of cleavages.

Scale Dependence

With the notion that the crystallographic defects are enhancing the compliance of biotite minerals, the relationship between the simulation, nanoindentation, and ultrasonic modulus can be understood as a result of scale-dependence. Wavelengths of ultrasonic waves at a megahertz frequency passing through minerals are typically on the order of few millimeters to a centimeter, which indicates that the indentation modulus based on ultrasonic measurements by Aleksandrov and Ryzhova (1961) represent the effective properties of biotites at such length scales. It is easy to perceive that a single crystal of few millimeters size contains defects, including cleavages, and the apparent stiffness of the crystal is lowered by those structural impurities. On the other hand, the mineral volume probed by the nanoindenter tips are at most several factors larger than the diameter of the indenter tip, approximately several μm for the 1 μm indenter, likely smaller than cleavage openings. However, because nanoindentation modulus is still consistently lower than the theoretical value of the defect-free mineral, this suggests that crystal defects are still prevalent and abundant features of the mineral influencing its mechanical properties at the sub-micron length scale.

4.4 Implications for deformation mechanisms in phyllosilicates

Dislocation glide along the (001) basal plane as a mechanism for creep in biotites have been studied extensively (Kronenberg et al., 1990; Christoffersen and Kronenberg, 1993), and Kronenberg et al. (1990) also determined the activation energies for two types of creep constitutive laws (i.e. exponential and power-law). However, dislocation glide does not accommodate any strain component parallel to the c-axis of the crystal structure, and what accommodates off-basal-plane plastic strain have remained ambiguous (Aslin et al., 2019). On the other hand, ripplocation as a ubiquitous deformation mechanism for layered solids (Barsoum et al., 2019) may also occur in phyllosilicates, allowing plastic deformation with a greater degree of freedom without fracturing the mineral by brittle deformation. This is because ripples in the basal layers give ripplocation a component strain parallel to the c-axis that is absent in basal dislocations (Aslin, 2019).

While plastic deformation of phyllosilicates by ripplocations have not been directly observed, whether such mechanism can accommodate the creep deformation of clay-minerals is of particular interest in crustal settings. It is known that clay-rich sedimentary rocks (e.g., shales) exhibit some time-dependent plastic deformational behavior even at low temperatures (Chang and Zoback, 2009; Sone and Zoback 2013, 2014a; Trzeciak et al., 2018). The importance of such creep behavior in characterizing the long-term behavior of subsurface reservoirs (Alramahi and Sundberg, 2012) and understanding origins of in-situ stress states in the crust is well-recognized (Warpinski, 1989; Gunzburger and Cornet, 2007; Sone and Zoback 2014b), but the exact physical mechanism causing the rock to creep is not clearly understood. Pore volume loss facilitated by grain sliding (i.e., compaction) is suggested to be an important mechanism for creep (Sone and Zoback, 2013, 2014a), but it is still undetermined if plastic deformation of the phyllosilicates minerals itself also contributes to the bulk rock creep behavior.

Deformation facilitated by ripplocations and its mechanical data, however, is still difficult to recover from mechanical testing at the scale of a single cleavage-free phyllosilicate crystal at the micron scale. If atomistic simulations therefore becomes an important technique in evaluating the potential for ripplocations to accommodate crystal plastic deformation, it will be crucial to properly incorporate the appropriate type and number of crystal defects in the models.

To this end, results from this study provide a benchmark for calibrating future atomistic models for phyllosilicate minerals.

5 Summary

We studied the elastic modulus of biotites using spherical nanoindentation and atomistic simulations. Our study uniquely reports the measured elastic properties of biotite using nanoindentation in two directions (layer-parallel and layer-normal loading). We also provide theoretical predictions of biotite elastic constants using density functional theory (DFT) not reported in the literature. We also propose a solution to estimate the indentation modulus (M) for spherical indentation from stiffness constants in an anisotropic material. Indentation modulus recovered from our nanoindentation results are generally equal to or higher than those recovered from dynamic ultrasonic measurements (Aleksandrov and Ryzhova, 1961), but lower than those predicted from the ideal defect-free DFT model. These differences highlight the presence of defects down to the nano-scale within naturally occurring phyllosilicates minerals, which may be important for understanding plastic deformation mechanism of phyllosilicates. Our results provide measured evidence that nano-scale defects affect the mechanical properties of phyllosilicate minerals.

Acknowledgments

This study was partially supported by scholarship and funding from the Indonesia Endowment Fund for Education (LPDP). We thank Connor Acker for the support in preparing the polished samples used in this study.

Data Availability Statement

Nanoindentation datasets for this research will be archived in MINDS@UW repository and are underway. Ultrasonic datasets for this research are included in Aleksandrov and Ryzhova (1961).

References

Ahmadov, R. (2011). Micro-textural, elastic and transport properties of source rocks, (Doctoral dissertation). Retrieved from Stanford Rock Physics & Borehole Geophysics Project. (https://srb.stanford.edu/microtextural-elastic-and-transport-properties-source-rocks). Stanford, CA: Stanford University.

Aleksandrov, K. S., & Prodaivoda, G. T. (1993). Elastic properties of minerals. *Crystallography reports*, 38(5), 698-709.

Aleksandrov, K. S., & Ryzhova, T. V. (1961). Elastic properties of rock-forming minerals II. Layered silicates. *Bulletin of the Academy of Sciences USSR, Geophysics Series, English translation*, 12, 1165-1168.

Alramahi, B., & Sundberg, M. I. (2012). *Proppant embedment and conductivity of hydraulic fractures in shales*. Paper presented at 46th U.S. Rock Mechanics / Geomechanics Symposium, Chicago, IL. ARMA-2012-291.

Aslin, J., Mariani, E., Dawson, K., & Barsoum, M. W. (2019). Ripplocations provide a new mechanism for the deformation of phyllosilicates in the lithosphere. *Nature Communication*, 10, 1-9. https://doi.org/10.1038/s41467-019-08587-2

Barnett, D. M., & Lothe, J. (1975). Line force loadings on anisotropic half-spaces and wedges. *Physica Norvegica*, 8, 13-22.

Barsoum, M. W., Zhao, X., Shanazarov, S., Romanchuk, A., Koumlis, S., Pagano, S. J., Lamberson, L., & Tucker, G. J. (2019). Ripplocations: A universal deformation mechanism in layered solids. *Physical Review Material*, 3, 013602. https://doi.org/10.1103/PhysRevMaterials.3.013602

Basu, S., Moseson, A., & Barsoum, M. W. (2006). On the determination of spherical nanoindentation stress-strain curves. *Journal of Materials Research*, 21(10), 2628-2637. https://doi.org/10.1557/jmr.2006.0324

Basu, S., Zhou, A., & Barsoum, M. W. (2009). On spherical nanoindentations, kinking nonlinear elasticity of mica single crystals and their geological implications. *Journal of Structural Geology*, 31, 791-801. https://doi.org/10.1016/j.jsg.2009.05.008

Bell, I. A., & Wilson (1986). TEM observations of defects in biotite and their relationship to polytypism. *Bulletin de Minéralogie*, 109(1-2), 163-170. https://doi.org/10.3406/bulmi.1986.7925

Blöchl, P. E. (1994). Projector augmented-wave method. *Physical Review B*, 50(24), 17953-17979. https://doi.org/10.1103/PhysRevB.50.17953

Bobko, C. P., Ortega, J. A., & Ulm, F. -J. (2009). Comment on “Elastic modulus and hardness of muscovite and rectorite determined by nanoindentation” by G. Zhang, Z. Wei & R. E. Ferrell [Applied Clay Science 43 (2009) 271-281]. *Applied Clay Science*, 46(4), 425-428. https://doi.org/10.1016/j.clay.2009.08.008

Bock, H., Dehandschutter, B., Martin, C. D., Mazurek, M., de Haller, A., Skoczylas, F., & Davy, C. (2010). *Self-sealing of fractures in argillaceous formations in the context of geological disposal of radioactive waste: Review and synthesis* (Rep. NEA-6184). Paris, France: Nuclear Energy Agency.

Brigatti, M. F., Frigieri, P., Ghezzo, C., & Poppi, L. (2000). Crystal chemistry of Al-rich biotites coexisting with muscovites in peraluminous granites. *American Mineralogist*, 85(3-4): 436-448. https://doi.org/10.2138/am-2000-0405

Broz, M. E., Cook, R. F., & Whitney, D. L. (2006). Microhardness, toughness, and modulus of Mohs scale minerals. *American Mineralogist*, 91(1), 135-142. https://doi.org/10.2138/am.2006.1844

Caddey, S. W., Bachman, R. L., Campbell, T. J., Reid, R. R., & Otto, R. P. (1991). The Homestake Gold Mine, An early Proterozoic Iron-Formation-Hosted Gold Deposit, Lawrence County, South Dakota. *U.S. Geological Survey Bulletin*, 1857.

Chang, C., & Zoback, M. D. (2009). Viscous creep in room-dried unconsolidated Gulf of Mexico shale (I): Experimental results. *Journal of Petroleum Science and Engineering*, 69, 239-246. https://doi.org/10.1016/j.petrol.2009.08.018

Christoffersen, R., & Kronenberg, A. K. (1993). Dislocation interactions in experimentally deformed biotite. *Journal of Structural Geology*, 15, 1077-1095. https://doi.org/10.1016/0191-8141(93)90157-6

Cygan, R. T., Liang, J. -J., & Kalinichev, A. G. (2004). Molecular models of hydroxide, oxyhydroxide, and clay phases and the development of a general force field. *The Journal of Physical Chemistry B*, 108(4), 1255-1266. https://doi.org/10.1021/jp0363287

Delafargue, A., & Ulm, F. -J. (2004). Explicit approximations of the indentation modulus of elastically orthotropic solids for conical indenters. *International Journal of Solids and Structures*, 41(26), 7351-7360. https://doi.org/10.1016/j.ijsolstr.2004.06.019

Dembicki, H., & Madren, J. D. (2014). Lessons learned from the Floyd shale play. *Journal of Unconventional Oil and Gas Resources*, 7, 1-10. https://doi.org/10.1016/j.juogr.2014.03.001

Domain C., & Monnet, G. (2005). Simulation of Screw Dislocation Motion in Iron by Molecular Dynamics Simulations. *Physical Review Letters*, 95, 215506. https://doi.org/10.1103/PhysRevLett.95.215506

Donohue, B. R., Ambrus, A., & Kalidindi, S. R. (2012). Critical evaluation of the indentation data analyses methods for the extraction of isotropic uniaxial mechanical properties using finite element models. *Acta Materialia*, 60(9), 3943-3952. https://doi.org/10.1016/j.actamat.2012.03.034

Field, J. S., & Swain, W. V. (1993). A simple predictive model for spherical indentation. *Journal of Materials Research*, 8(2), 297-306. https://doi.org/10.1557/JMR.1993.0297

Field, J. S., & Swain, W. V. (1996). The indentation characterisation of the mechanical properties of various carbon materials: Glassy carbon, coke and pyrolytic graphite. *Carbon*, 34(11), 1357-1366. https://doi.org/10.1016/S0008-6223(96)00071-1

Gale, J. D. (1997). GULP: a computer program for the symmetry adapted simulation of solids. *Journal of the Chemical Society, Faraday Transactions*, 93(4), 629-637. https://doi.org/10.1039/A606455H

Grimme, S., Antony, J., Ehrlich, S., & Krieg, H. (2010). A consistent and accurate ab initio parametrization of density functional dispersion correction (DFT-D) for the 94 elements H-Pu. *The Journal of Chemical Physics*, 132(15), 154104. https://doi.org/10.1063/1.3382344

Grimme, S., Ehrlich, S., & Goerigk, L. (2011). Effect of the damping function in dispersion corrected density functional theory. *Journal of Computational Chemistry*, 32(7), 1456-1465. https://doi.org/10.1002/jcc.21759

Gunzburger, Y., & Cornet, F. H. (2007). Rheological characterization of a sedimentary formation from a stress profile inversion. *Geophysical Journal International*, 168, 402-418. https://doi.org/10.1111/j.1365-246X.2006.03140.x

Haghighat, E., Rassouli, F. S., Zoback, M. D., & Juanes, R. (2020). A viscoplastic model of creep in shale. *Geophysics*, 85(3), MR155-MR166. https://doi.org/10.1190/geo2018-0700.1

Herbert, E. G., Pharr, G. M., Oliver, W. C., Lucas, B. N., & Hay, J. L. (2001). On the measurement of stress-strain curves by spherical indentation. *Thin Solid Films*, 398-399, 331-335. https://doi.org/10.1016/S0040-6090(01)01439-0

Hertz, H. (1881). On the contact of elastic solids, *Journal für die reine und angewandte Mathematik*, 92, 156-171. Translated and reprinted in English in Hertz's Miscellaneous Papers (1896), 146-162, London, England: Macmillan and Co.

Hysitron (2014). nanoDMA III user manual, Revision 9.4.0914.

Ingram, G. M., Urai, J. L. (1999). Top-seal leakage through faults and fractures: The role of mudrock properties. *Geological Society of London, Special Publications*, 158(1), 125-135. https://doi.org/10.1144/GSL.SP.1999.158.01.10

Johnson, K. L. (1985). *Contact mechanics*. Cambridge, England: Cambridge University Press. https://doi.org/10.1017/CBO9781139171731

Kalidindi S. R., & Pathak, S. (2008). Determination of the effective zero-point and the extraction of spherical nanoindentation stress-strain curves. *Acta Materialia*, 56(14), 3523-3532. https://doi.org/10.1016/j.actamat.2008.03.036

Karato, S. (2008). *Deformation of earth materials: An introduction to the rheology of solid earth*. New York, NY: Cambridge University Press. https://doi.org/10.1017/CBO9780511804892

Kresse, G., & Furthmüller, J. (1996). Efficiency of ab-initio total energy calculations for metals and semiconductors using a plane-wave basis set. *Computational Materials Science*, 6(1), 15-50. https://doi.org/10.1016/0927-0256(96)00008-0

Kronenberg, A. K., Kirby, S. H., & Pinkston, J. (1990). Basal slip and mechanical anisotropy of biotite. *Journal of Geophysical Research: Solid Earth*, 95(B12), 19257-19278. https://doi.org/10.1029/JB095iB12p19257

Kushima, A., Qian, X., Zhao, P., Zhang, S., & Li, J. (2015). Ripplocations in van der Waals Layers. *Nano Letters*, 15, 1302-1308. https://doi.org/10.1021/nl5045082

Lanin, E. S., Acker, C., Yu, Z., Sone, H., & Wang, B. (2019). Comparing biotite elastic properties recovered by nano-indentation with molecular simulation predictions. Paper presented at 53rd US Rock Mechanics / Geomechanics Symposium, New York, NY. ARMA 19-1803.

Li, X., & Bhushan, B. (2002). A review of nanoindentation continuous stiffness measurement technique and its applications. *Materials Characterization*, 48 (1), 11-36. https://doi.org/10.1016/S1044-5803(02)00192-4

Mavko, G., Mukerji, T., & Dvorkin, J. (2009). *The rock physics handbook, Second Edition: Tools for Seismic Analysis of Porous Media*. New York, NY: Cambridge University Press. https://doi.org/10.1017/CBO9780511626753

Militzer, B., Wenk, H. -R., Stackhouse, S., & Stixrude, L. (2011). First-principles calculation of the elastic moduli of sheet silicates and their application to shale anisotropy. *American Mineralogist*, 96(1), 125-137. https://doi.org/10.2138/am.2011.3558

Moseson, A. J., Basu, S., & Barsoum, M. W. (2008). Determination of the effective zero point of contact for spherical nanoindentation. *Journal of Materials Research*, 23(1), 204-209. https://doi.org/10.1557/JMR.2008.0012

Noe, D. C., & Veblen, D. R. (1999). HRTEM analysis of dislocation cores and stacking faults in naturally deformed biotite crystals. *American Mineralogist*, 84(11-12), 1925-1931. https://doi.org/10.2138/am-1999-11-1220

Oldenburg. C. M., Dobson, P. F., Wu, Y., Cook, P. J., Kneafsey, T. N., Nakagawa, S., et al. (2016) *Intermediate-scale hydraulic fracturing in deep mine kISMET project summary 2016* (Rep. LBNL-1006444). Berkeley, CA: Lawrence Berkeley National Laboratory.

Oldenburg. C. M., Dobson, P. F., Wu, Y., Cook, P. J., Kneafsey, T. N., Nakagawa, S., et al. (2017) *Hydraulic fracturing experiments at 1500 m depth in a deep mine: Highlights from the kISMET project*. Paper presented at 42nd Workshop on Geothermal Reservoir Engineering, Stanford, CA

Oliver, W. C., & Pharr, G. M. (1992). An improved technique for determining hardness and elastic modulus using load and displacement sensing indentation experiments. *Journal of Materials Research*, 7(6), 1564-1583. https://doi.org/10.1557/JMR.1992.1564

Oliver, W. C., & Pharr, G. M. (2004). Measurement of hardness and elastic modulus by instrumented indentation: Advances in understanding and refinements to methodology. *Journal of Materials Research*, 19(1), 3-20. https://doi.org/10.1557/jmr.2004.19.1.3

Pathak, S., Shaffer, J., & Kalidindi, S. R. (2009). Determination of an effective zero-point and extraction of indentation stress-strain curves without the continuous stiffness measurement signal. *Scripta Materialia*, 60(6), 439-442. https://doi.org/10.1016/j.scriptamat.2008.11.028

Pathak, S., & Kalidindi, S. R. (2015). Spherical nanoindentation stress–strain curves. *Materials Science and Engineering R*, 91, 1-36. https://doi.org/10.1016/j.mser.2015.02.001

Perdew, J. P., Burke, K., & Ernzerhof, M. (1996). Generalized gradient approximation made simple. *Physical Review Letters*, 77(18), 3865-3868. https://doi.org/10.1103/PhysRevLett.77.3865

Poirier, J. (1985). *Creep of crystals: High-temperature deformation processes in metals, ceramics and minerals*. New York, NY: Cambridge University Press. https://doi.org/10.1017/CBO9780511564451

Sone, H., & Zoback, M. D. (2013). Mechanical properties of shale-gas reservoir rocks - Part 2: Ductile creep, brittle strength, and their relation to the elastic modulus. *Geophysics*, 78(5), D393-D402. https://doi.org/10.1190/geo2013-0051.1

Sone, H., & Zoback, M. D. (2014a). Time-dependent deformation of shale gas reservoir rocks and its long-term effect on the in-situ state of stress. *International Journal of Rock Mechanics and Mining Science*, 69, 120-132. https://doi.org/10.1016/j.ijrmms.2014.04.002

Sone, H., & Zoback, M. D. (2014b). Viscous relaxation model for predicting least principal stress magnitudes in sedimentary rocks. *Journal of Petroleum Science and Engineering*, 124, 416-431. https://doi.org/10.1016/j.petrol.2014.09.022

Swadener, J. G., & Pharr, G. M. (2001). Indentation modulus of elastically anisotropic half-spaces by cones and parabolae of revolution. *Philosophical Magazine A*, 81(2), 447-466. https://doi.org/10.1080/01418610108214314

Tabor, D. (1951). *Hardness of Metals*. London, England: Oxford University Press.

Teich-McGoldrick, S. L., Greathouse, J. A., & Cygan, R. T. (2012). Molecular dynamics simulations of structural and mechanical properties of muscovite: Pressure and temperature effects. *The Journal of Physical Chemistry C*, 116(28), 15099-15107. https://doi.org/10.1021/jp303143s

Trzeciak, M., Sone, H., & Dabrowski, M. (2018). Long-term creep tests and viscoelastic constitutive modeling of lower Paleozoic shales from the Baltic Basin, N Poland. International *Journal of Rock Mechanics and Mining Sciences*, 112, 139-157. https://doi.org/10.1016/j.ijrmms.2018.10.013

Vaughan, M. T., & Guggenheim, S. (1986). Elasticity of muscovite and its relationship to crystal structure. *Journal of Geophysical Research: Solid Earth*, 91(B5), 4657-4664. https://doi.org/10.1029/JB091iB05p04657

Vigilante, P. J., Sone, H., Wang H. F., Haimson, B., & Doe, T. W. (2017). Anisotropic strength of Poorman Formation rocks, kISMET Project. Paper presented at 51st US Rock Mechanics / Geomechanics Symposium, San Francisco, CA. ARMA 17-766.

Vlassak, J. J., & Nix, W. D. (1993). Indentation modulus of elastically anisotropic half spaces. *Philosophical Magazine A*, 67(5), 1045-1056. https://doi.org/10.1080/01418619308224756

Vlassak, J. J., & Nix, W. D. (1994). Measuring the elastic properties of anisotropic materials by means of indentation experiments. *Journal of the Mechanics and Physics of Solids*, 42(8), 1223-1245. https://doi.org/10.1016/0022-5096(94)90033-7

Vlassak, J. J., Ciavarella, M., Barber, J. R., & Wang, X. (2003). The indentation modulus of elastically anisotropic materials for indenters of arbitrary shape. *Journal of the Mechanics and Physics of Solids*, 51(9), 1701-1721. https://doi.org/10.1016/S0022-5096(03)00066-8

Vyzhva, S. A., Prodayvoda, G. T., & Vyzhva, A. S. (2014). Elastic properties of some clay minerals. *Nafta-Gaz*, 11, 743-756.

Warpinski, N.R. (1989). Elastic and viscoelastic calculations of stresses in sedimentary basins. *SPE Formation Evaluation*, 4(4), 522-530. https://doi.org/10.2118/15243-PA

Willis, J. R. (1966). Hertzian contact of anisotropic bodies. *Journal of the Mechanics and Physics of Solids*, 14, 163-176. https://doi.org/10.1016/0022-5096(66)90036-6

Whitney, D. L., Broz, M., & Cook, R. F. (2007). Hardness, toughness, and modulus of some common metamorphic minerals. *American Mineralogist*, 92(2-3), 281-288. https://doi.org/10.2138/am.2007.2212

Yamakov, V., Wolf, D., Phillpot, S. R., Mukherjee, A. K., & Gleiter, H. (2002). Dislocation processes in the deformation of nanocrystalline aluminium by molecular-dynamics simulation. *Nature Materials*, 1, 45-49. https://doi.org/10.1038/nmat700

Zhang, G., Wei, Z., & Ferrell, R. E. (2009). Elastic modulus and hardness of muscovite and rectorite determined by nanoindentation. *Applied Clay Science*, 43(2), 271-281. https://doi.org/10.1016/j.clay.2008.08.010

Zhang, G., Wei, Z., Ferrell, R. E., Guggenheim, S., Cygan, R. T., & Luo, J. (2010). Evaluation of the elasticity normal to the basal plane of non-expandable 2:1 phyllosilicate minerals by nanoindentation. *American Mineralogist*, 95(5-6), 863-869. https://doi.org/10.2138/am.2010.3398